

Highly oriented semiconducting polymer nanofilm with enhanced crystallinity

Received: 25 March 2025

Accepted: 21 October 2025

Published online: 27 November 2025

 Check for updates

Wenhai Xie^{1,3}, Quanzheng Deng^{1,3}, Jibiao Wu¹, Fangsen Li^②, Wenyang Dan¹, Xuefeng Wang^①✉, Lu Han^①✉ & Hongbo Gu^①✉

Semiconducting polymers are crucial in flexible and wearable intelligent organic electronic devices. However, their crystallization remains a significant challenge because the crystallization kinetics is limited by the rigid conjugation structure and strong intermolecular π - π stacking. This leads to energetic disorder in electronic structure and poor charge transport, which severely hinders electrical performances of devices. Herein, we report highly oriented semiconducting polymers with enhanced crystallinity prepared by low-temperature plasma-driven evaporation process, during which polymer chains cross the energy barrier and crystallization kinetic for approaching torsion-free conformations. This material possesses an extended intrachain conjugation, ordered interchain stacking, high crystallinity and narrowed density of states contribution, which causes the extraordinary electrical response to stimulations with the emphatic Seebeck coefficient and power factor 1017% and 8295% times those of spin-coated film, respectively.

Semiconducting polymers have been extensively explored as candidates in flexible and wearable intelligent electronic devices for their great advantages of low budget, lightweight, and mechanical flexibility^{1,2}. The electrical performances of these devices largely depend on the molecular ordering in the solid state. It is reported that the intrinsically structural disorder in conventional semiconducting polymers from the coiled conformation of polymer chains results in the energetic disorder in electronic structure, forming the Gaussian distribution for the density of states (DOS)³. Therefore, it is tremendously necessary to synthesize the high-crystalline semiconducting polymer to reduce the energetic disorder and optimize their electronic structure⁴. However, the torsion and entanglement of chains in semiconducting polymers with rigid conjugation backbone and strong π - π stacking interaction create an insurmountable activation energy and kinetic barrier to the rearrangement of chain conformation, leading to a complex free energy landscape with multiple energetic barriers for crystallization^{5–7}. So far, the crystals of semiconducting polymers like polyaniline (PANI), polypyrrole (PPy), and poly(3-alkythiophenes) have been achieved through vapor phase polymerization or solution process methods^{8,9}. However, the

controllable fabrication of large-area semiconducting polymers nanofilm with enhanced crystalline structure remains a long-standing challenge, which severely limits the industrial application of semiconducting polymers in the electronic device. Recently, the crystallization of PANI was realized relying on the hydrogen bonding and electrostatic interactions from surfactant monolayer in the interfacial polymerization^{10–12}, while their growth rate was quite slow (~5 nm per day) and the thickness of film was limited under 30 nm. As the thickness became thicker, gradually surpassing the interface, the interactions from surfactant monolayer were weakened, possibly leading to the formation of abundant defects and damaging the crystallization¹³. Unfortunately, the fundamental thermodynamic and kinetic issues in the crystallization of common semiconducting polymers have not been solved.

Herein, we report highly oriented semiconducting polymers with enhanced crystallinity synthesized by low-temperature plasma stemmed from the modified resonant infrared matrix assisted pulse laser evaporation technique (RIR-MAPLE). By receiving the low-phonon energy of laser, the polymer chains in vapor phase have crossed the energy barriers and crystallization kinetic and been rearranged from

¹Shanghai Key Lab of Chemical Assessment and Sustainability, School of Chemical Science and Engineering, Tongji University, Shanghai, PR China. ²Vacuum Interconnected Nanotech Workstation, Suzhou Institute of Nano-Tech and Nano-Bionics, Chinese Academy of Sciences (CAS), Suzhou, PR China. ³These authors contributed equally: Wenhai Xie, Quanzheng Deng. ✉e-mail: xfwang@tongji.edu.cn; luhan@tongji.edu.cn; hongbogu2014@tongji.edu.cn

their preferred metastable coiled conformation to the stable torsion-free state in the vacuum circumstance. This leads to the deposition of a high-crystalline semiconducting polymer nanofilm with high sensitivity and response towards stimulations from light, magnetism and heat.

Results

Design and preparation of highly oriented semiconducting polymers

As illustrated in Fig. 1a, the RIR-MAPLE technique is modified with the adoption of a rotating reflector for the uniform laser ablation, during which a laser ablates a frozen target consisting of solvent and polymer, and the evaporated polymer is deposited on a substrate. Initially, the dispersing agent poly(styrenesulfonate) (PSS) was introduced to form a well-dissolved PANI methanol (with low sticking coefficient) solution for guaranteeing the stretching state of PANI chains (digital photos in Supplementary Fig. 1a), as ascertained by the isotropic wide-angle X-ray scattering (WAXS) pattern in Supplementary Fig. 2. Then the frozen target was instantly attained by liquid nitrogen, in which the PANI chains were immobilized with the stretchable conformation. After being ablated by the laser pulse, the solvent methanol molecules absorbed most of the laser energy, since their O-H stretching vibration bear a resonance enhancement by the laser with the matched wavelength of 1064 nm in the near infrared region, and leave the surface of the frozen target to form the plume. In this situation, the embedded polymers were intactly transferred into the plasma plume because of the collisions between the solvent and polymer as pictured in the digital photos of Supplementary Fig. 3, ultimately stacked on the substrate with the stretching conformation.

During deposition, PSS was designedly removed from the system to avoid them from squeezing into the orderly stacking of PANI chains, damaging the crystalline structure and reducing the moisture stability. According to the density functional theory (DFT) simulation results in Fig. 1b, there is a strong electrostatic attraction between PSS and proton-doped PANI chains, but weak interaction between PSS and de-doped PANI. Hereby, the separation of PSS was obtained by partially de-doping the PANI via the laser-induced plasma¹⁴, as detailed described in Supplementary Note 2. Finally, PSS was successfully removed from the system by the strong hydrogen bonding with methanol, justified by the high-resolution X-ray photoelectron spectroscopy (XPS) S 2p spectra in Fig. 1c, d. Subsequently, the deposition of PANI chain was monitored by the atomic force microscope-infrared spectrum (AFM-IR) mode of infrared scanning near-field optical microscopy (SNOM) in Fig. 1e, f and Supplementary Fig. 4. The elaborate deposition stages at different deposition time of 10, 20, 30 and 40 min are emphasized in Supplementary Note 3. It was worth noting that after extending the deposition time over 40 min, the bending chain conformation appeared and caused the accumulative structural disorder, as shown in Supplementary Fig. 5. The nondestructive deposition of PANI chains has been ensured from the minor difference between relative molecular weight of PANI in the nanofilm (75806 Da) and raw material (73186 Da) obtained by the gel permeation chromatograph (GPC) of Supplementary Fig. 6. The chemical structures of PANI including oxidation unit (i.e., quinone ring) and reduction unit (i.e., benzene ring) are well preserved in the nanofilm as examined by the Fourier transform infrared (FTIR) spectra in Supplementary Fig. 7a, Raman spectra in Supplementary Fig. 7b, ¹H nuclear magnetic resonance (¹H-NMR) spectra¹⁵ in Supplementary Fig. 8 and high resolution XPS N 1s spectra in Supplementary Fig. 9, whose characteristic peaks

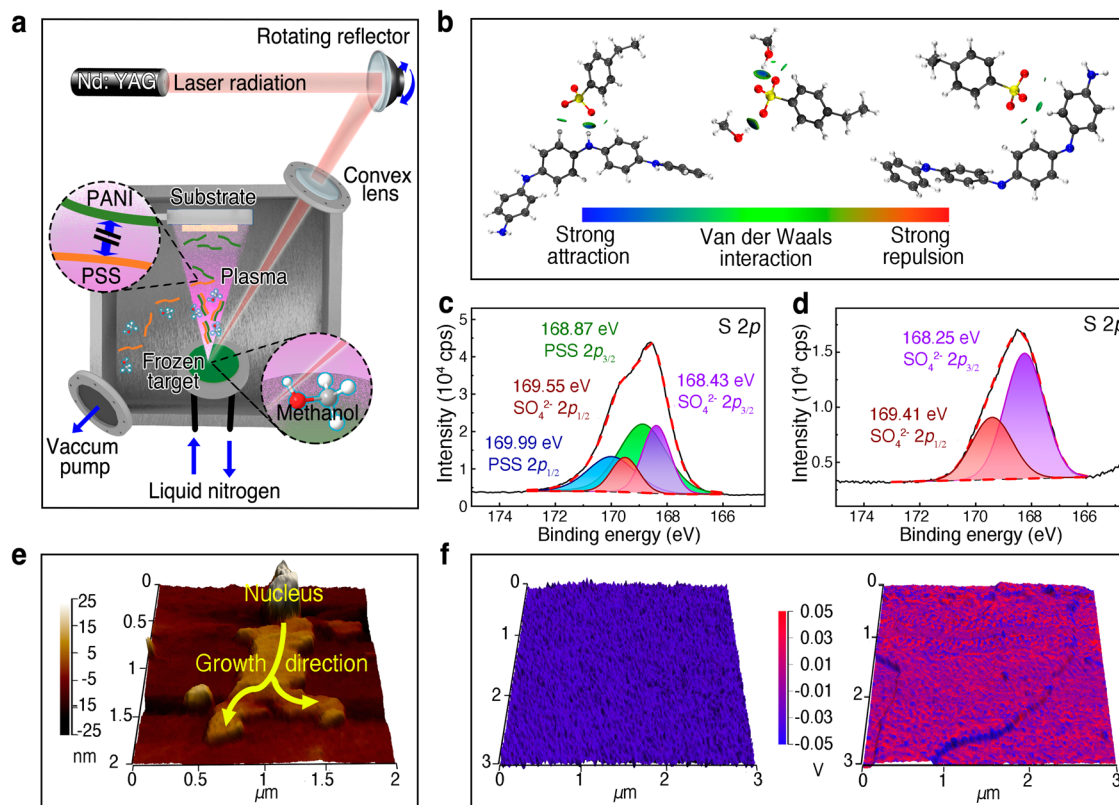


Fig. 1 | Preparation of the highly oriented semiconducting polymer nanofilm. a Brief scheme of customized RIR-MAPLE instrument for semiconducting polymer nanofilm deposition. b DFT simulations imply the strong electrostatic attraction between PSS and proton-doped PANI (left), weak correlation between PSS and de-doped PANI (right), and strong hydrogen bonding

between PSS and methanol (middle). High-resolution XPS S 2p spectra of c doped PANI bulk and d partially de-doped PANI nanofilm. e AFM image connotes the deposition process of the PANI nanofilm. f AFM-IR images of substrate (left) and the PANI nanofilm at early deposition stage (right) captured by SNOM.

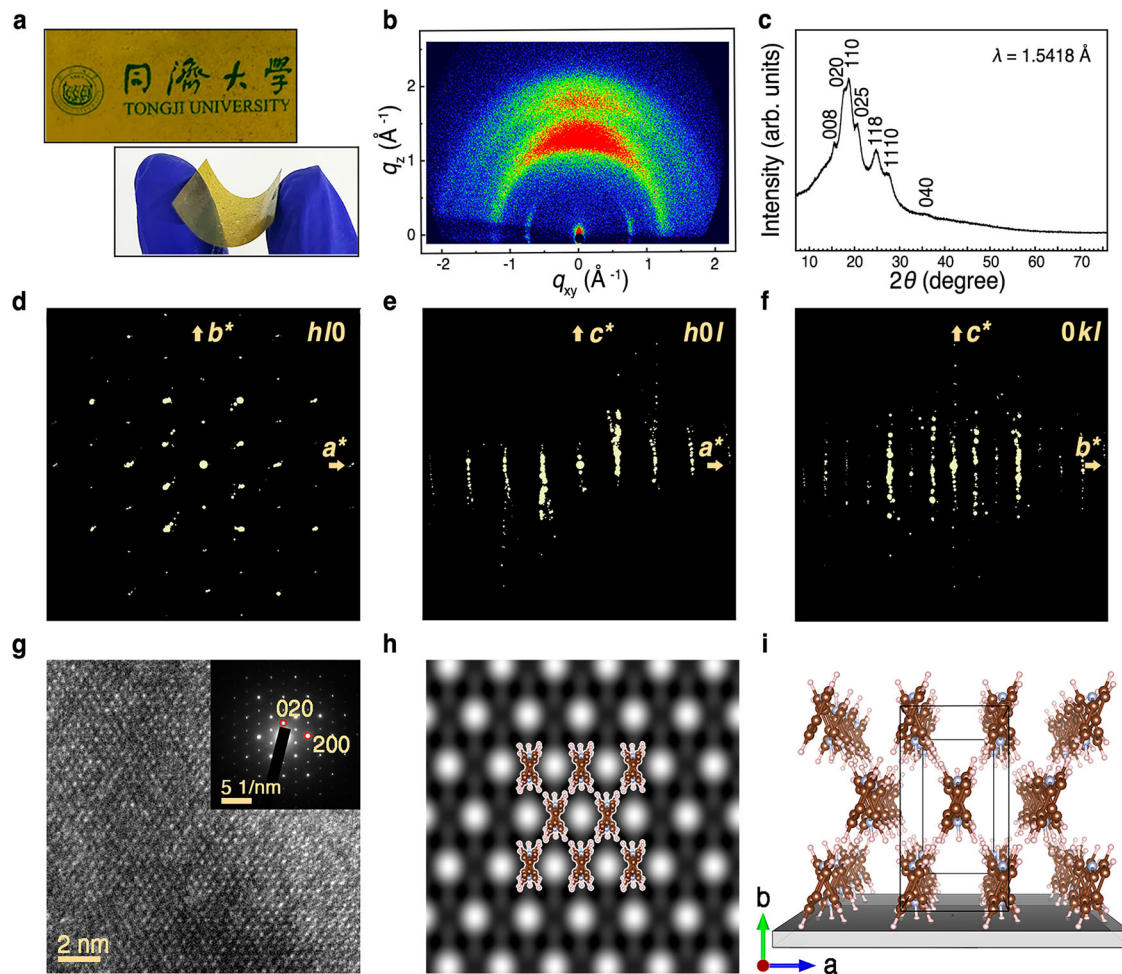


Fig. 2 | Structural characterizations. **a** Digital photos of the PANI nanofilm, showing its transparency properties (top) and flexibility when bent (bottom), respectively. **b** WAXS pattern of the PANI nanofilm, which displays anisotropic intensity between in-plane (q_{xy}) and out-of-plane (q_z) directions. **c** GIXRD pattern of PANI nanofilm. **d–f** 2D slices of 3D reciprocal lattice of PANI reconstructed from the 3D-ED data shown from c^* , b^* and a^* axes, respectively. **g** HRTEM image and

corresponding SAED pattern of the PANI nanofilm taken from c -axes. **h** Symmetry averaged HRTEM image obtained from Fig. 2g with structural models of polymer chains overlaid upon. **i** Schematic drawing of the crystalline structure and growing direction of PANI chains along with the substrate. The corresponding crystallographic information file is provided in Supplementary Data 1.

were summarized in Supplementary Table 1 and percentage were calculated in Supplementary Table 2. Within the laser-induced plasma, the PANI chains could go through a rearrangement into the most stable state with alternating ranking of oxidation and reduction units¹⁶, as listed in the DFT simulation results in Supplementary Fig. 10a.

Characterizations

Relying on our carefully organized strategy, a uniform, transparent and flexible nanofilm of semiconducting polymers has been produced at deposition time of 10 min and visualized in Fig. 2a. The morphology of the nanofilm shows a homogeneous appearance with an average relative transparency of 92.5% in the visible light region compared to the yellow polyimide (PI) substrate, identified from the ultraviolet-visible (UV-Vis) spectra in Supplementary Fig. 11. The nanofilm signals a uniform morphology with surficial fibrous protrusions in the transmission electron microscopy (TEM) image of Supplementary Fig. 12. This neat PANI layer tightly attaches to the PI substrate, delineating the thickness of 100 nm and the average roughness of 34.5 nm from the scanning electron microscope (SEM) and atomic force microscopy (AFM) images in Supplementary Figs. 13 and 14, respectively.

WAXS pattern shown in Fig. 2b indicates the orientation and polymer chain conformation in the nanofilm, which manifests the sharp peaks of strong out-of-plane scattering and relatively weak in-

plane scattering. The peaks identified from $I(q)$ - q profiles in Supplementary Fig. 15 deduced from Fig. 2b are summarized in Supplementary Table 3, supporting the edge-on orientations of polymer chains in the nanofilm¹⁷. The radius of gyration (R_g) of 17.01 Å and fractal dimension (D_f) of 2.01 calculated from Fig. 2b in Supplementary Table 4 clarify the elongated Gaussian chain state upon the nanofilm¹⁸, comparable to the chain conformation in the methanol solution with a R_g of 9.88 Å and D_f of 1.22 obtained from Supplementary Fig. 2. The grazing incidence X-ray diffraction (GIXRD) pattern in Fig. 2c displays the relatively sharp reflection intensity. Combined with TEM investigations (*vide post*), the structure exhibits an orthorhombic unit cell with lattice parameter of $a = 5.35$ Å and $b = 9.99$ Å. Nevertheless, a large c axis along the polymer chain axis is determined, as corroborated by the low-angle XRD result under transmission mode, as presented in Supplementary Fig. 16d, in which a broad intensity distribution in the 2θ region of 1.74–2.19° indicates that the c axis varies from 40.28 to 50.74 Å. The characteristic peaks of PANI with emeraldine salt (ES) state is summarized in Supplementary Table 5. In term of the equation in Supplementary Note 1, the crystallinity of polymers in nanofilm is estimated to be 89.3%. GIXRD pattern is also exploited to derive the grain size (L) and interchain separation length (R), and the results are summarized in Supplementary Table 6. Generally, a larger L value benefits the intrachain charge carriers transport along with the

conjugate backbone and a lower R value improves the probability of interchain hopping of charge carriers^{19,20}. In Supplementary Table 6, the intrachain transport of charge carriers is ameliorated in our nanofilm with the L value of 81.0 nm relative to that of 41.2 nm for the spin-coated film, conforming the increasing conjugation length of polymer chain. By contrast, the R value in our nanofilm with a value of 5.8 nm shows a slight difference relative to that of 5.4 nm for the spin-coated film.

In order to further confirm the crystalline structure, the PANI nanofilm was peeled off from the substrate, and data were collected employing the three-dimensional electron diffraction (3D-ED) technique. Figure 2d-f shows the projection of the reconstructed 3D reciprocal lattice from c^* , b^* and a^* axes of PANI nanofilm, respectively. The 3D-ED data show discrete diffraction spots consistent with single crystal diffraction, while the diffraction intensity and the fluctuation in their position may be from the uneven length of polymer chain segments along the polymer chain direction (c -axis), that possibly cause the dislocation and defect in the crystal of polymer as well as formation of amorphous phase. Particularly, the $hk0$ reflections are well ordered, while the $00l$ reflections tend to be positionally deviated and have a more diffuse intensity distribution, indicating that the PANI chain is well arranged in the ab plane but shows less ordering in the long-axis of polymer chain (c -axis). Although the diffuse diffraction intensity and positional shifts along the c^* -axis pose challenges in determining the extinction rules, the typical reflection conditions of $\{hkl: h + k = 2n\}$, $\{hk0: h + k = 2n\}$, $\{h00: h = 2n\}$ and $\{0k0: k = 2n\}$ suggest a potential C -centered orthorhombic lattice. The unit cell parameters of $a = 5.3 \text{ \AA}$, $b = 10.0 \text{ \AA}$ and $c = 45.2 \text{ \AA}$ are determined, which align well with the XRD results (Fig. 2c and Supplementary Fig. 16d). However, the obtained 3D-ED data are not sufficient to resolve the structure in molecular level due to the imperfections in the crystallization of polymer chains and the presence of structural fluctuations. Therefore, we further analyzed the structure through high-resolution TEM (HRTEM) imaging. The representative HRTEM image with the corresponding selected area electron diffraction (SAED) pattern taken from the c -axis is shown in Fig. 2g, showing mm symmetry with centered structure as suggested from the extinction conditions. The unit cell parameters calculated from the SAED pattern are $a = 5.3 \text{ \AA}$ and $b = 10.0 \text{ \AA}$, which are consistent with the XRD and 3D-ED results. The average structural information was obtained from Fourier transformation of the HRTEM image (Fig. 2g) using the crystallographic image processing software CRISP²¹, suggesting the plane group symmetry of $c2mm$ (Fig. 2h). The black contrast indicates the areas with high electrostatic potential density, corresponding to the positions of the polymer chain. Since the arrangement of polymer chains is not as ordered as that of atomic crystals, we can only observe the overall electrostatic potential density distribution considering each polymer chain as a whole. Based on the averaged projected potential, the $C2mm$ (No. 38) is suggested to be the most possible space group symmetry. However, to establish the structural model, we utilized $P1$ symmetry and then the chain configurations were optimized by using the DFT method in the Vienna ab initio simulation package (VASP) for energy minimization. As shown in Fig. 2i, the growing direction of PANI nanofilm is along the substrate, and it is stagger-stacked in the form of a C -centered orthorhombic structure. While the packing of polymer chain is more random in the direction of chain extension. In this structure, the interchain distance from 3.8 to 4.2 \AA suggests the strong π - π stacking and implies the edge-on orientation of PANI chain with the benzene ring perpendicular to the substrate, which is also confirmed by WAXS results²². The simulated SAED, XRD and 3D-ED profiles derived from the structural model shown in Supplementary Fig. 16a-d and Supplementary Movie 1 display concordance with aforementioned experimental results, which proves the reliability of this model. In addition, large-scale TEM image and corresponding SAED patterns taken from large area of the film in Supplementary Fig. 16e demonstrate a consistent and uniform

structure with single-crystalline characteristic within the nanofilm with clear lattice fringes and discrete diffraction spots. Crystalline grains with blue fluorescence response were also observed in the nanofilm through fluorescence microscope images as shown in Supplementary Fig. 16f. By contrast, the film prepared from the common spin-coating method only discloses a crystallinity of 45.5%, whose results are listed in Supplementary Note 4.

Electronic structure and electrical transport properties

By managing the chain conformation, orientation, and crystallinity in semiconducting polymer, its energetic disorder has been cut down to a degree. The electronic structure of the polymer in nanofilm was measured from the superconducting quantum interference device (SQUID) magnetometry and ultraviolet photoelectron spectroscopy (UPS). The SQUID magnetometry was employed to conduct the temperature-dependent magnetic susceptibility data ($\chi-T$) in Fig. 3a. The PANI nanofilm uncovers a weak temperature-dependent paramagnetic property in the temperature range of 100–300 K, where Pauli paramagnetic susceptibility (χ_p) and the DOS at the Fermi level ($N(E_F)$) have been acquired from the linear $\chi T-T$ plot as inset of Fig. 3a²³. As described above, the DOS of semiconducting polymers normally follows the Gaussian distribution centered at the Fermi level. Our nanofilm gains a much higher $N(E_F)$ of $2.72 \times 10^{23} \text{ state eV}^{-1} \text{ m}^{-3}$, compared with that of $9.28 \times 10^{21} \text{ state eV}^{-1} \text{ m}^{-3}$ for the spin-coated film, which implies the narrowed DOS distribution of our nanofilm. Besides, the electronic structure of nanofilm also brings about unique fluorescence emission around 500 nm (2.48 eV) under the excitation wavelength of 325 nm (3.81 eV), which is unseen in the spin-coated film, as illustrated in the right of Fig. 3b. This might be due to the narrower band gap of 1.82 eV in nanofilm compared with that of 1.95 eV in spin-coated film, calculated from UV-Vis spectra in left of Fig. 3b and listed in Supplementary Table 7. The $N(E_F)$ of the PANI nanofilm is also sensitive to the magnetic field, as listed in Supplementary Table 8, which is increased from 5.69×10^{23} to $2.30 \times 10^{24} \text{ state eV}^{-1} \text{ m}^{-3}$ when magnetic field \mathbf{B} reaches 3 T, which means that the DOS distribution in nanofilm become narrower under the magnetic field. For comparison, the $N(E_F)$ of spin-coated film only exhibits a slight increase from 1.38×10^{22} to $2.75 \times 10^{22} \text{ state eV}^{-1} \text{ m}^{-3}$ in the same condition. From the UPS spectra in Supplementary Fig. 17, the work function (Φ) has been computed and listed in Supplementary Table 9. The lower Φ of 6.45 eV in nanofilm, relative to 7.76 eV of the spin-coated film, makes a better interface matching with the metal electrodes due to the declined potential barrier, which promotes the charge carrier transport and electrical performance within the electronic device based on our nanofilm, see details in Supplementary Note 6-(2). Moreover, the values of the $N(E_F)$ and Φ in Fig. 3c express an obvious size-dependency toward the thickness of nanofilm. This denotes that the electronic structure of nanofilm could be easily regulated by its thickness, i.e., deposition time. It is noticed that with extending deposition time, the structural disorder is accumulated in the nanofilm from the formed several deep channels by ablating the frozen target of laser as illustrated in Supplementary Fig. 18. To solve this issue, our modified MAPLE still needs to be upgraded in the future.

The excellent physical structure and electronic structures accelerate the charge carrier transport within the PANI nanofilm. The temperature-dependent electrical conductivity ($\sigma-T$) is determined in the inset of Fig. 3d, from which the reduced activation energy (W) has been derived²⁴. In line with the temperature-independent $W-T$ plot in Fig. 3e, our nanofilm lies in the critical regime of metal-insulator transition below 200 K. In this condition²⁵, the $\sigma-T$ curve follows the power law of $\sigma(T) \propto T^\beta$ with β value of 0.49. At temperature over 200 K, $W-T$ plot with positive slope implies that the PANI nanofilm crosses from the critical regime to the metallic regime, illustrating the metallic transport behavior of nanofilm. The dominant contribution of Pauli paramagnetism possessed from the

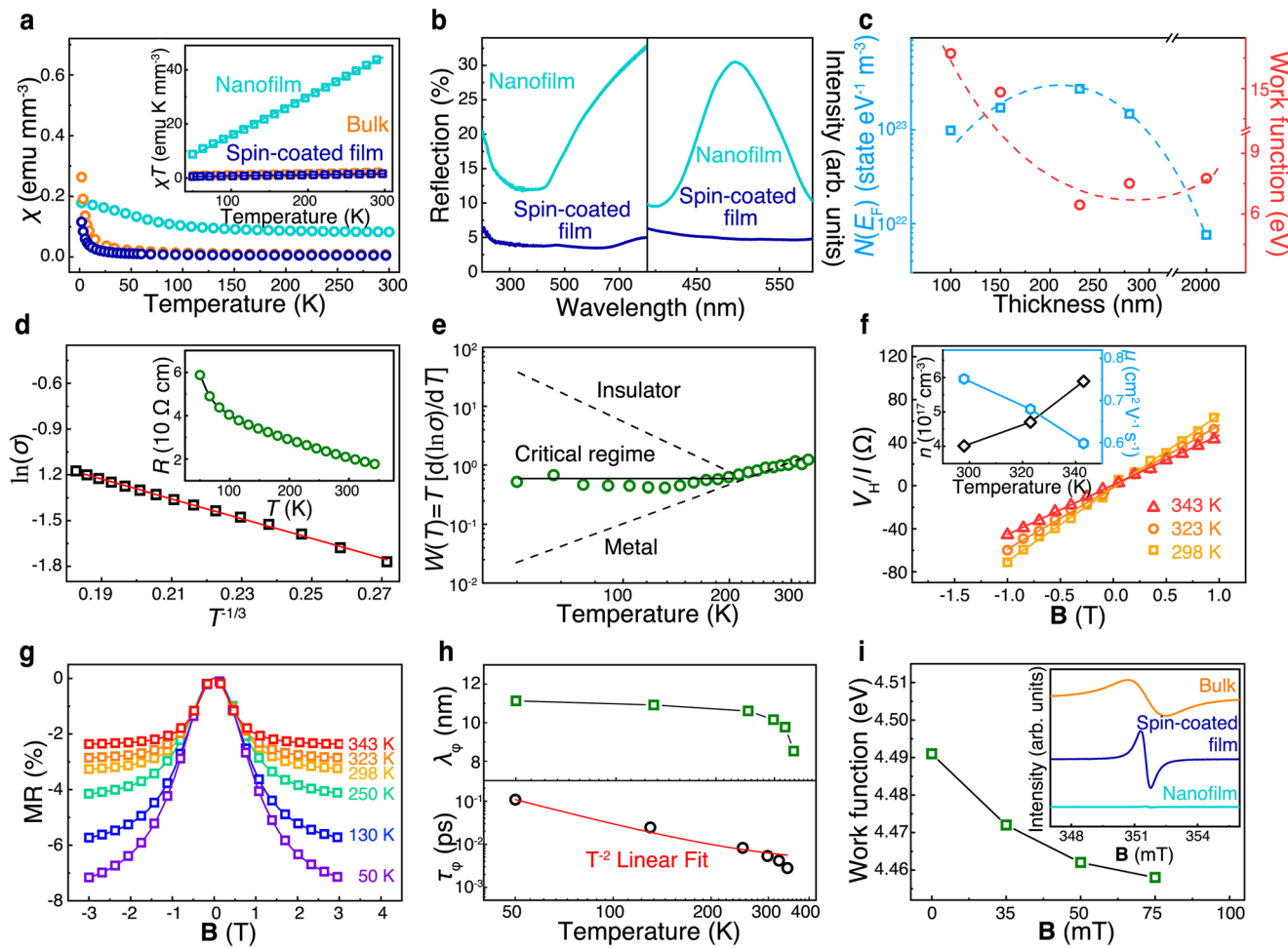


Fig. 3 | Electronic structure and transport properties. **a** Temperature (T) dependence of magnetic susceptibility (χ) under the magnetic field \mathbf{B} of 1 T. Inset is the linear fitting of χT - T plot. **b** UV (left) and fluorescence (right) spectra of nanofilm and spin-coated film. **c** Size-dependent density of states at Fermi level ($N(E_F)$) and work function of the nanofilm relative to the spin-coated film with a thickness of 2 μm . **d** Plot of $\ln(\sigma)$ - $T^{-1/3}$ fitting from the temperature-dependent resistance (R - T) of the nanofilm (inset), σ stands for electrical conductivity. **e** Plot of W - T for nanofilm by using double logarithmic coordinate axis, W represents

reduced activation energy. The dash line exhibits the characteristic of insulator and metal. **f** Hall resistance (V_H/I) measured at different temperatures for nanofilm. Insets are the calculated charge carrier density (n) and mobility (μ) in the nanofilm. **g** Magnetoresistance (MR) of the nanofilm at various temperatures. **h** Temperature dependence of inelastic scattering length λ_ϕ (top) and time τ_ϕ (bottom) extracted from magnetoresistance. **i** Magnetic field (\mathbf{B}) dependent work function of the PANI nanofilm extracted from KPFM surface potential. Insets are EPR spectra of nanofilm compared with spin-coated film and bulk.

χT - T plot in Supplementary Table 10 expresses the delocalized nature of charge carriers in our nanofilm, which manifests the metallic coherent charge transport as well. This behavior recommends the unique quantum effect in the nanofilm, since the spin-coated film prefers the insulator regime originated from the negative slope of W - T plot in Supplementary Fig. 19f. Moreover, since our nanofilms still exhibit the characteristics of imperfect crystallization of the polymer chain as confirmed by 3D-ED data above, Mott variable range hopping (VRH) theory (see Supplementary Note 1) is adopted to process the σ - T data and explore the mechanism of charge transport in the semiconducting polymer film. Our nanofilm (Fig. 3d) displays a fitting parameter of $x=3$ (Supplementary Table 11), designating a quasi-2D Mott VRH mechanism for the charge carrier transport behavior. For comparison, a 3D VRH mechanism ($x=4$) is noticed in the spin-coated film from Supplementary Fig. 19e. Testing under the four-probe method, our nanofilm holds an electrical conductivity up to 1.71 S cm^{-1} . The charge carrier density of our nanofilm is worked out to be $4.01 \times 10^{17} \text{ cm}^{-3}$ and the room temperature Hall mobility reaches $0.75 \text{ cm}^2 \text{ V}^{-1} \text{ s}^{-1}$ by Hall effect measurement, as demonstrated in Fig. 3f and Supplementary Table 12. Clear Hall signal is transcribed in a wide

temperature range from 298 to 343 K and the positive slope for the linear plot of V_H/I - \mathbf{B} coincides to the *p*-type doping.

The metallic coherent charge transport is also consistent with the negative magnetoresistance (MR) phenomenon in a wide temperature range with increasing absolute value of MR as the temperature decreases, as exhibited in Fig. 3g. This phenomenon could be explained through the weak localization effect, which arises from the coherent backscattering when a constructive interference happens between charge waves opposite transferring along closed paths with equal probabilities²⁶. The magnetic field would break this balance and reduce the backscattering, further enhancing the electrical conductivity²⁷. The MR data have been processed by the simplified Hikami–Larkin–Nagaoka model from the weak spin-orbit coupling assumption, see details in Supplementary Note 1, where the inelastic scattering time (τ_ϕ) and length (λ_ϕ) are received and recorded in Fig. 3h. The larger τ_ϕ and λ_ϕ could be found at low temperatures, which intimates the increased degree of charge coherence and agrees with the rising MR value²⁸. Furthermore, the temperature-dependent τ_ϕ against T^2 depicts clearly that the electron-electron scattering acts as a dominant scattering mechanism²⁹. Successively, in-situ Kelvin probe force microscope

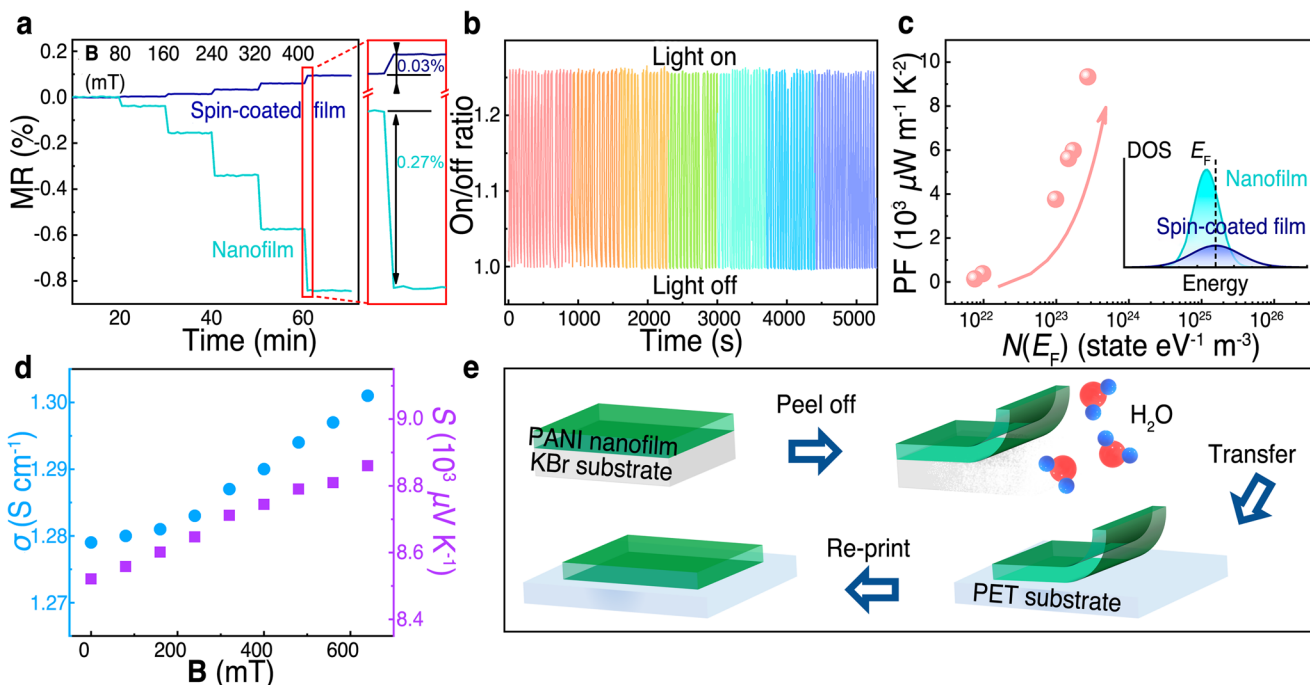


Fig. 4 | Applications and stability. **a** Magnetoresistance (MR) sensitivity of nanofilm and spin-coated film under weak magnetic field. **B**. **b** Nanofilm displays stable photoconductivity signal under 100 on/off cycles. **c** Correlation between the density of states (DOS) at Fermi level ($N(E_F)$) and thermoelectric power factor (PF)

of the nanofilm. Inset is the illustrated electronic structure of DOS near the Fermi level (E_F). **d** Positive MTE phenomenon in the PANI nanofilm, in which σ is electrical conductivity, S is Seebeck coefficient. **e** Schematic illustration for water-assisted transfer of freestanding PANI nanofilm.

(KPFM) has been carried out under magnetic field for scanning the surface potentials of our nanofilm, as arranged in Supplementary Fig. 20 and Supplementary Movie 2. With \mathbf{B} increasing to 75 mT, the surface potential of nanofilm is gradually decreased without obviously surface morphology altering in Supplementary Fig. 20. The estimated surficial ϕ of our nanofilm evinces a downturn in Fig. 3i, signifying the boosted charge carrier transport under the magnetic field, which testifies to the occurrence of spin current in the PANI nanofilm under magnetic field³⁰.

The MR property also affirms the conversion of charge carriers between polaron and bipolaron in accordance with the bipolaron theory^{31,32}. Spinless bipolaron is ascertained to be the major charge carrier in the nanofilm, since its electron paramagnetic resonance (EPR) spectrum in inset of Fig. 3i barely exhibits signal. For comparison, the strong intensity in EPR spectrum of spin-coated film hints the dominance of polaron. The localization length (a_0) derived from MR data in Supplementary Table 8 is also coincided with the conjugation of polymer chain and formation of bipolaron in the PANI nanofilm, since its a_0 of 83.0 nm is much larger than that of spin-coated film (13.2 nm).

Applications and stability

The single-crystalline structure and metallic coherence charge transport have brought our semiconducting polymeric nanofilm great potential in applications within the electronic nanodevices. Primarily, the sensor properties towards magnetic or optical signal are discussed. Under the \mathbf{B} of 3 T, the room-temperature negative MR with a value of -3.2% was detected in the nanofilm, while a more usual positive MR phenomenon with a value of 1.8% was discerned for the spin-coated film under the same condition (Supplementary Fig. 21a). It is also noted that the nanofilm also gains high MR sensitivity of 3.38% T⁻¹ under low magnetic field, nine times higher than that of spin-coated film (0.37% T⁻¹), as shown in Fig. 4a. The photoconductivity was also assessed under the Xenon lamp, as explicated in Fig. 4b and Supplementary Fig. 21b, c. The PANI nanofilm exhibits a stable signal during 100 on/off

cycles and the highest on/off ratio of 2.59, which is 1.8 times of that for spin-coated film (1.44).

The thermoelectric performance of the PANI nanofilm was also evaluated. Our nanofilm reveals an excellent thermoelectric capability with the highest power factor (PF) up to 9328.2 $\mu\text{W m}^{-1} \text{K}^{-2}$ due to a high Seebeck coefficient of 8544.0 $\mu\text{V K}^{-1}$. By contrast, the PF for spin-coated film only reaches 103.1 $\mu\text{W m}^{-1} \text{K}^{-2}$ since its Seebeck coefficient is 840.2 $\mu\text{V K}^{-1}$. It is obvious that the PF and Seebeck coefficient of our nanofilm are 83.0 and 10.2 times those of the spin-coated film, respectively. The thermoelectric voltage output of the PANI nanofilm is also stable among a wide temperature range, as mentioned in Supplementary Fig. 21d. Our nanofilm shows very high thermoelectric performance in comparison with published works, as listed in Supplementary Table 13. The much higher $N(E_F)$ and increasing bipolaron in our nanofilm relative to spin-coated film denotes the narrow DOS shape, enhanced DOS slope at E_F and increased asymmetry³³, according to the inset of Fig. 4c. From the positive correlation between the $N(E_F)$ and effective mass of charge carrier (m^*) in Supplementary Note 1, the ratio of m^* between the nanofilm and spin-coated film is calculated to be 10.9, close to the ratio of their Seebeck coefficient of 10.2. Referring to the correlation of PF ~ $N(E_F)$ in Fig. 4c, it is declared that the growth of the $N(E_F)$ in our nanofilm leads to the larger m^* , further raising the Seebeck coefficient. The enlargement of m^* could be fundamentally originated from the strengthened electron-photon coupling interaction by the formation of aforementioned bipolaron in the semiconducting polymer³⁴.

Furthermore, an interesting positive magneto-thermoelectric (MTE) phenomenon was discovered in our nanofilm. The voltage output of thermoelectric device demonstrates a step-up tendency in Supplementary Fig. 21e under the rising magnetic field strength. Eventually, the Seebeck coefficient increases to 8860.2 $\mu\text{V K}^{-1}$, and the PF value achieves 10213.2 $\mu\text{W m}^{-1} \text{K}^{-2}$ under \mathbf{B} of 680 mT, as explained in Supplementary Table 14. This maybe the reason that on one hand, the negative MR brings the rising of electrical conductivity under the magnetic field. On the other hand, the enlarged m^* derived from the

magnified $N(E_F)$ under magnetic field in Supplementary Table 8 leads to the promotion of Seebeck coefficient³⁵. This brings the decoupling and simultaneous amelioration of electrical conductivity and Seebeck coefficient under magnetic field, as illustrated in Fig. 4d.

Our PANI nanofilm owns a superb moisture stability resulting from the designed removal of PSS, which prevents the moisture-derived degradation of electronic device³⁶. As revealed in Supplementary Fig. 22a, the PANI nanofilm exhibits the electrical conductivity and Seebeck coefficient with minor difference during a 30-day period when being packaged into a thermoelectric device, characterized as Supplementary Fig. 22b. After being immersed in water for one week, the surface of our nanofilm displays no obvious damage and the microstructure observed by SEM is still tidy in Supplementary Fig. 23. Based on the exceptional moisture stability, a water-assisted transfer printing becomes possible by depositing PANI nanofilm upon a soluble substrate (e.g., KBr panel) as drawn in Fig. 4e and Supplementary Fig. 22c. The whole PANI nanofilm is quickly peeled off when the substrate is disintegrated in water. Then, the free-standing nanofilm could be completely re-printed upon an untreated PET substrate, maintaining its transparency. This feature makes convenience for the coating of semiconducting polymer nanofilm upon irregular substrate³⁷.

Generality

The generality of our strategy is proved in different semiconducting polymers like polypyrrole. Since the PSS was removed during the RIR-MAPLE process, as proved by XPS in Supplementary Fig. 24, the PPy nanofilm exposes a good crystalline structure as well with a large-scale crystallographic lattice fringe in HRTEM image of Supplementary Fig. 25. In a word, our strategy could manipulate the chain conformation and crystalline structure in semiconducting polymers.

Discussion

In this article, we report highly oriented semiconducting polymers with extended localization length, narrowed DOS contribution and metallic coherent charge transport behavior, by using the low-temperature plasma-driven evaporation in the modified RIR-MAPLE. Our material gains extraordinary electrical responses to thermal, magnetic and optical stimulations, and exhibits a positive MTE, in which the decoupled electrical conductivity and Seebeck coefficient perform simultaneous rising under magnetic field. This work offers an insight for the realizing of highly oriented semiconducting polymers with superior electrical performances, which is a promising candidate in state-of-the-art next-generation organic electronic devices like organic thin film transistors (OTFT) in the aspect of chip industry to get rid of the photolithography process.

Methods

Materials

Aniline (C_6H_5N , ≥99.5%) and ammonium persulfate (APS, ≥98.0%) were purchased from Aladdin Reagent (Shanghai) Co., Ltd. Poly(sodium-*p*-styrenesulfonate) (PSS, M_w = 70000) was obtained from Shanghai Macklin Biochemical Co., Ltd. Sulfuric acid (95.0–98.0%), ammonia (25.0–28.0%), acetone (≥99.5%) and methanol (≥99.5%) were supplied by Sinopharm Chemical Reagents Co., Ltd. All chemicals were used as received without any pre-treatment.

Synthesis of polyaniline

Aniline was added into sulfuric acid solution with an aniline to sulfate mole ratio of 1:2.5 under sonication until the formed salt was well dissolved. PSS was dispersed in deionized water with an aniline to PSS mass ratio of 0.9:1 under mechanical stirring (300 rpm) for 1 h. Two solutions above were mixed firstly, followed by the addition of APS solution with an aniline to APS mole ratio of 1:1. Reaction system was kept in an ice-water bath with continuous mechanical stirring and

sonication for 2 h. Lastly, acetone of equal volume was added into the reaction system and the product was filtrated and dried to obtain soluble PANI/PSS (PANI bulk). Insoluble polyaniline (PANI) was also manufactured with the same procedure without addition of PSS.

Fabrication of polyaniline nanofilm by RIR-MAPLE process

The target solution (2 wt%) was prepared by dissolving PANI bulk in methanol under sonication. About 5 mL of solution was loaded in the target cup in the nitrogen atmosphere, which was then rapidly cooled in liquid nitrogen until the solution was completely frozen at about -120 °C. The polyimide substrate (PI, thickness of 25 μm) was attached to a holder. The target cup was installed inside the RIR-MAPLE chamber with a target-to-substrate distance of 3 cm. The chamber was then quickly evacuated using a pump (TRP-24, Beijing Beiyi Woosung Vacuum Technology Co., Ltd) and the vacuum degree was maintained at a magnitude of 10^{-1} Pa during the deposition process. The Nd: YAG laser (Quanta-Ray Lab, λ = 1064 nm, Spectra-Physics) was set with an energy density of 294 mJ per pulse and focused on a tiny spot upon the target through a clockwise rotating reflector (6 rad min⁻¹). Throughout deposition, the target was kept at a temperature range around -150 to -170 °C, monitored by a thermocouple, and the substrate was kept at 50 °C by heating with a laser radiation (λ = 808 nm, FC-W-808-50W, Changchun New Industries Optoelectronics Tech Co., Ltd). The deposition was carried out for 30 min and the obtained film was called Untreated PANI nanofilm. After that, the Untreated PANI nanofilm was annealed at 150 °C for 12 h in the nitrogen atmosphere with a gas flow rate of 20 mL min⁻¹ by using a tube furnace. The attained film was indexed as Annealed PANI nanofilm. Finally, Annealed PANI nanofilm was immersed in the 20 mL of sulfuric acid (1 M) with 3 h for the secondary doping process and taken out for drying. This sample was named as NF-30. For comparison, the different deposition times for 10, 20, and 40 min were also performed with the same procedure and the samples were labeled as NF-10, NF-20, and NF-40 min, respectively.

Characterizations

The microstructures and morphologies of PANI nanofilm were observed by a field emission scanning electron microscope (SEM, Hitachi S-4800), high-resolution transmission electron microscopy (HRTEM, FEI Tecnai G2-F30 and JEOL JEM-F200) and atomic force microscope (AFM, Bruker Dimension Icon). During TEM testing, the 3D electron diffraction (3D-ED) data were collected at a low dose mode at 298 K on a Synergy-ED and equipped with a HyPix-ED electron detector under 200 kV. For the PANI nanofilm, 244 ED patterns were collected with the tilting angle ranging from -55° to 60°. Each frame was collected with an exposure time of 0.750 s, resulting in a 0.43° wedge per frame. The 3D reciprocal space was reconstructed using the program CrystalAlis^{Pro} for ED. Surface phases were analyzed by infrared scanning near-field optical microscopy (SNOM, Bruker NanoIR3-s) in the AFM-IR mode at a wavenumber of 1308 cm⁻¹ that is representative for the C-N stretching vibration of benzenoid in PANI. The grazing incidence X-ray diffraction (GIXRD) patterns were identified through X-ray diffractometer (Bruker D8 Advance) with Cu K α 1 ($h\nu$ = 8.05 keV) radiation. Wide angle X-ray scattering (WAXS) patterns were tested by Xenocs Xeuss 3.0 beamline with Cu K α 1 radiation in grazing incidence mode. X-ray photoelectron spectroscopy (XPS) was recorded on a Thermo ESCALAB 250Xi spectrometer respectively with Al K α ($h\nu$ = 1486.6 eV) radiation. Ultraviolet photoelectron spectroscopy (UPS) was recorded on a Thermo ESCALAB 250Xi spectrometer, respectively with He I ($h\nu$ = 21.20 eV) radiation. Thermal properties of samples are analyzed by a thermogravimetric analyzer (TGA, TA Instruments, TGA 55) and differential scanning calorimeter (DSC, TA Instruments, DSC 25). Fourier transform infrared spectroscopy (FTIR) was analyzed by an infrared spectrometer (Thermo Nicolet NEXUS) and ultraviolet-visible spectroscopy (UV-Vis) was carried out with an ultraviolet-visible-near infrared spectrometer (Agilent Technologies, Carry 5000).

Fluorescence spectrum (FL) was collected by fluorescence spectrometer (Hitachi F-7000). The Raman spectroscopy was carried out with a Raman spectrometer (Invia 514 nm, Renishaw Inc.). The molecular weight of polymer was evaluated with gel permeation chromatograph (GPC, Shimadzu GPC-20A) and the PANI in nanofilm was dissolved by dimethyl sulfoxide (DMSO). ¹H Nuclear magnetic resonance (¹H-NMR) spectra were recorded by Bruker AVANVVE III (400 MHz) using DMSO d6 as solvent. Temperature-dependent magnetic susceptibility was carried out on a superconducting quantum interference device (SQUID, MPMS SQUID XL5, Quantum Design). The electron paramagnetic resonance (EPR) spectroscopy was recorded by Bruker A300-10/12. Morphology and surface potential of PANI nanofilm under an external magnetic field (**B**) were detected by using Kelvin probe force microscope (KPFM, Bruker Dimension Icon) with a HQ:NC18/Pt tip, whose work function was confirmed as 4.33 eV referring to a highly oriented pyrolytic graphite (4.60 eV).

Electrical performance measurements

Electrical conductivity of PANI nanofilm was tested with a digital source meter (Keithley 2400) through the four-point probe method. To assemble a thermoelectric device, PANI nanofilm was cut into size of 2.5 × 1.5 cm and packaged with two Pt electrodes by the plastic envelop machine. The heat side of device was attached to the outside wall of a copper tank containing continuously heated water and cold side was exposed to the air. The temperature difference (ΔT) was monitored by a thermocouple. The output voltage (ΔV) under different ΔT was recorded using an electrostatic meter/high resistance meter (Keithley 6517B) by changing the temperature of the heat side from 20 to 60 °C. The Seebeck coefficient was obtained from the linear fitting of ΔT - ΔV plot. The thermoelectric results were also examined using Seebeck coefficient measurement system (Advance Riko ZEM-3M8). For MTE test, the aforementioned testing procedure of thermoelectric performance was carried out in a custom-made electromagnet, with thermoelectric device perpendicular to the magnetic field. Photoconductivity performance was measured by putting the packaged nanofilm under the illumination from a Xenon lamp (BBZM-1), whose full power was 470 W and full illuminance was 5800 lx. The output current of device was recorded using a digital source meter (Keithley 2400) with input voltage of 5 V. Temperature-dependent resistivity, Hall effect and MR tests were performed with a physical property measurement system (Quantum Design PPMS-9T (EC-II)) at different temperatures. Please see detailed temperature in the results of Fig. 3d, f, g, respectively. The MR performance of nanofilm was tested under a step-wise raised magnetic field with a step length of 80 mT.

Data availability

All data supporting the results of this study are available in the manuscript and its Supplementary Information. All data are available from the corresponding author upon request. Source data are provided with this paper.

References

1. Wang, S.-J. et al. Highly efficient modulation doping: a path toward superior organic thermoelectric devices. *Sci. Adv.* **8**, eabl9264 (2022).
2. Chen, C. et al. Observation of weak counterion size dependence of thermoelectric transport in ion exchange doped conducting polymers across a wide range of conductivities. *Adv. Energy Mater.* **13**, 2202797 (2023).
3. Abutaha, A. et al. Correlating charge and thermoelectric transport to paracrystallinity in conducting polymers. *Nat. Commun.* **11**, 1737 (2020).
4. Deng, S. et al. High-performance and ecofriendly organic thermoelectrics enabled by n-type polythiophene derivatives with doping-induced molecular order. *Adv. Mater.* **36**, 2309679 (2024).
5. Liang, Z. et al. N-type charge transport in heavily p-doped polymers. *Nat. Mater.* **20**, 518–524 (2021).
6. Boyle, C. J. et al. Tuning charge transport dynamics via clustering of doping in organic semiconductor thin films. *Nat. Commun.* **10**, 2827 (2019).
7. Karki, A. et al. Unifying energetic disorder from charge transport and band bending in organic semiconductors. *Adv. Funct. Mater.* **29**, 1901109 (2019).
8. Jiang, Y., Liu, T. & Zhou, Y. Recent advances of synthesis, properties, film fabrication methods, modifications of poly(3,4-ethylenedioxithiophene), and applications in solution-processed photovoltaics. *Adv. Funct. Mater.* **30**, 2006213 (2020).
9. Puthirath, B. et al. Exceptionally crystalline and conducting acid doped polyaniline films by level surface assisted solution casting approach. *Appl. Phys. Lett.* **108**, 161901 (2016).
10. Zhang, T. et al. Two-dimensional polyaniline crystal with metallic out-of-plane conductivity. *Nature* **638**, 411–417 (2025).
11. Ballabio, M. et al. Band-like charge transport in phytic acid-doped polyaniline thin films. *Adv. Funct. Mater.* **31**, 2105184 (2021).
12. Seki, T. et al. Real-time study of on-water chemistry: Surfactant monolayer-assisted growth of a crystalline quasi-2D polymer. *Chem* **7**, 2758–2770 (2021).
13. Zhang, T. et al. Engineering crystalline quasi-two-dimensional polyaniline thin film with enhanced electrical and chemiresistive sensing performances. *Nat. Commun.* **10**, 4225 (2019).
14. Xu, J., Chen, D. & Meng, S. Probing laser-induced plasma generation in liquid water. *J. Am. Chem. Soc.* **143**, 10382–10388 (2021).
15. Giri, H., Ma, G., Almtiri, M., Gu, X. & Scott, C. N. Side chain effects on the conductivity of phenothiazine-derived polyaniline. *Chem. Mater.* **36**, 2279–2288 (2024).
16. Scaccabarozzi, A. D. et al. Doping approaches for organic semiconductors. *Chem. Rev.* **122**, 4420–4492 (2022).
17. Sarabia-Riquelme, R. et al. Highly conductive n-type polymer fibers from the wet-spinning of n-doped PBDF and their application in thermoelectric textiles. *Adv. Funct. Mater.* **34**, 2311379 (2024).
18. Yu, Z.-D. et al. Buffer chain model for understanding crystallization competition in conjugated polymers. *Angew. Chem. Int. Ed.* **63**, e202405139 (2024).
19. Kang, S. D. & Snyder, G. J. Charge-transport model for conducting polymers. *Nat. Mater.* **16**, 252–257 (2017).
20. Xiao, M. et al. Achieving ideal transistor characteristics in conjugated polymer semiconductors. *Sci. Adv.* **9**, eadg8659 (2023).
21. Hovmöller, S. CRISP: crystallographic image processing on a personal computer. *Ultramicroscopy* **41**, 121–135 (1992).
22. Wang, R.-R. et al. Micropattern of silver/polyaniline core-shell nanocomposite achieved by maskless optical projection lithography. *Nano Lett.* **22**, 9823–9830 (2022).
23. Ji, X. et al. Pauli paramagnetism of stable analogues of pernigraniline salt featuring ladder-type constitution. *J. Am. Chem. Soc.* **142**, 641–648 (2020).
24. Gueye, M. N., Carella, A., Faure-Vincent, J., Demadrille, R. & Simonato, J.-P. Progress in understanding structure and transport properties of PEDOT-based materials: A critical review. *Prog. Mater. Sci.* **108**, 100616 (2020).
25. Onozuka, K. et al. Metallic state of a mixed-sequence oligomer salt that models doped PEDOT family. *J. Am. Chem. Soc.* **145**, 15152–15161 (2023).
26. Fu, S. et al. Outstanding charge mobility by band transport in two-dimensional semiconducting covalent organic frameworks. *J. Am. Chem. Soc.* **144**, 7489–7496 (2022).
27. Liu, K. et al. A quasi-2D polypyrrole film with band-like transport behavior and high charge-carrier mobility. *Adv. Mater.* **35**, 2303288 (2023).
28. Wang, D., Yu, H., Shi, W. & Xu, C. Chemical doping of organic and coordination polymers for thermoelectric and spintronic

applications: a theoretical understanding. *Acc. Chem. Res.* **56**, 2127–2138 (2023).

- 29. Kang, K. et al. 2D coherent charge transport in highly ordered conducting polymers doped by solid state diffusion. *Nat. Mater.* **15**, 896–902 (2016).
- 30. Keene, S. T. et al. Efficient electronic tunneling governs transport in conducting polymer-insulator blends. *J. Am. Chem. Soc.* **144**, 10368–10376 (2022).
- 31. Ding, S. et al. Organic single-crystal spintronics: magnetoresistance devices with high magnetic-field sensitivity. *ACS Nano* **13**, 9491–9497 (2019).
- 32. LeCroy, G. et al. Using molecular structure to tune intrachain and interchain charge transport in indacenodithiophene-based copolymers. *J. Am. Chem. Soc.* **146**, 21778–21790 (2024).
- 33. Ju, D., Kim, J., Yook, H., Han, J. W. & Cho, K. Engineering counter-ion-induced disorder of a highly doped conjugated polymer for high thermoelectric performance. *Nano Energy* **90**, 106604 (2021).
- 34. Dai, R. et al. Molecular single crystals induce chain alignment in a semiconducting polymer. *Adv. Compos. Hybrid. Mater.* **6**, 35 (2023).
- 35. Zhao, W., Ding, J., Zou, Y., Di, C. -a & Zhu, D. Chemical doping of organic semiconductors for thermoelectric applications. *Chem. Soc. Rev.* **49**, 7210–7228 (2020).
- 36. Jiang, Y. et al. An alcohol-dispersed conducting polymer complex for fully printable organic solar cells with improved stability. *Nat. Energy* **7**, 352–359 (2022).
- 37. Aivali, S., Beaumont, C. & Leclerc, M. Conducting polymers: towards printable transparent electrodes. *Prog. Polym. Sci.* **148**, 101766 (2024).

Acknowledgements

H.G. acknowledges support from the National Natural Science Foundation of China (51703165), Shanghai Rising-Star Program (19QA1409400), Fundamental Research Funds for Central Universities, and Shanghai Science and Technology Commission (19DZ2271500). L.H. acknowledges support from the National Natural Science Foundation of China (22425303) and the Fundamental Research Funds for Central Universities. X.W. acknowledges support from the National Natural Science Foundation of China (22273066). The authors are grateful for the technical support from Nano-X in Suzhou Institute of Nano-Tech and Nano-Bionics, Chinese Academy of Sciences (SINANO). The authors thank Prof. Zhang Zengxing in Fudan University for the assistance in sample processing and the measurement of electrical performance, Ms. Kong Lulu in Tongji University for the recording of fluorescence spectrum, and Prof. Zhang Zhenjie in Nankai University for the support in 3D-ED data collection. The authors thank SCI-GO for the SQUID analysis. The WAXS test was supported by Beijing Zhongkebaice Technology Service Co., Ltd (www.zkbaice.cn). The authors thank Ceshihui (www.cephihui.cn) for the XPS analysis.

Author contributions

H.G. and X.W. initiated the concept, designed the project, guided the study, analyzed the results, and revised the manuscript. L.H. guided the study, analyzed the results, and revised the manuscript. W.X. prepared the samples, carried out the general characterization and property measurements, analyzed the data, and wrote the draft manuscript. Q.D. carried out the TEM characterization, analyzed the data, and assisted in the visualization of data. J.W. prepared the samples and assisted in the visualization of data. W.D. assisted in the analysis of TEM and XRD data. F.L. assisted in the AFM and SNOM measurement and analyzed the data. All the author approved the final version of the manuscript.

Competing interests

The authors declare no competing interests.

Additional information

Supplementary information The online version contains supplementary material available at <https://doi.org/10.1038/s41467-025-65709-9>.

Correspondence and requests for materials should be addressed to Xuefeng Wang, Lu Han or Hongbo Gu.

Peer review information *Nature Communications* thanks Ju-Won Jeon, Hui Li, and Dhandapani Venkataraman for their contribution to the peer review of this work. A peer review file is available.

Reprints and permissions information is available at <http://www.nature.com/reprints>

Publisher's note Springer Nature remains neutral with regard to jurisdictional claims in published maps and institutional affiliations.

Open Access This article is licensed under a Creative Commons Attribution-NonCommercial-NoDerivatives 4.0 International License, which permits any non-commercial use, sharing, distribution and reproduction in any medium or format, as long as you give appropriate credit to the original author(s) and the source, provide a link to the Creative Commons licence, and indicate if you modified the licensed material. You do not have permission under this licence to share adapted material derived from this article or parts of it. The images or other third party material in this article are included in the article's Creative Commons licence, unless indicated otherwise in a credit line to the material. If material is not included in the article's Creative Commons licence and your intended use is not permitted by statutory regulation or exceeds the permitted use, you will need to obtain permission directly from the copyright holder. To view a copy of this licence, visit <http://creativecommons.org/licenses/by-nc-nd/4.0/>.

© The Author(s) 2025